Far-infrared vibration–rotation-tunneling spectroscopy of Ar–NH_3: Intermolecular vibrations and effective angular potential energy surface

C. A. Schmuttenmaer, R. C. Cohen, J. G. Loeser, and R. J. Saykally
Department of Chemistry, University of California, and Materials and Chemical Sciences Division, Lawrence Berkeley Laboratory, Berkeley, California 94720

(Received 10 January 1991; accepted 21 March 1991)

Two new intermolecular vibration–rotation-tunneling (VRT) bands of Ar–NH_3 have been measured using tunable far infrared laser spectroscopy. We have unambiguously assigned these and a previously measured FIR band [Gwo *et al.*, Mol. Phys. **71**, 453 (1990)] as $\Pi(1_0,n=0) \leftarrow \Sigma(0_0,n=0)$, $\Sigma(1_0,n=0) \leftarrow \Sigma(0_0,n=0)$, and $\Sigma(0_0,n=1) \leftarrow \Sigma(0_0,n=0)$. The three upper states of these are found to be strongly mixed by anisotropy and Coriolis effects. A simultaneous least squares fit of all transitions has yielded vibrational frequencies, rotational and centrifugal distortion constants, and a Coriolis parameter as well as quadrupole hyperfine coupling constants for the upper states. An effective angular potential energy surface for Ar–NH_3 in its lowest stretching state has been determined from these data, after explicitly accounting for the effects of bend stretch interactions. Features of the surface include a global minimum at the near T-shaped configuration ($\theta = 90°$), a 30 cm^{-1} to 60 cm^{-1} barrier to rotation at $\theta = 180°$ (or 0°), and a very low barrier or possibly a secondary minimum at $\theta = 0°$ (or 180°). Both attractive and repulsive interactions are shown to contribute significantly to the anisotropic forces in the complex. Comparison with *ab initio* calculations are presented.

I. INTRODUCTION

It is now well known that the large amplitude motions and dynamical couplings characteristic of weakly bound molecules often render the familiar concepts of equilibrium structures, normal modes, and rovibrational separability, essentially useless for quantitatively describing their spectra and properties. One can more effectively comprehend the properties and dynamics of weakly bound clusters as proceeding directly from the multidimensional intermolecular potential energy surface (PES) and associated wave functions without any intervening dynamical assumptions. Although such a description is indeed far more difficult to formulate and to implement, the proliferation of modern supercomputers and the development of new and very efficient computational methods actually makes this approach quite practical for systems of low dimensionality. For example, Hutson[1] employed a close-coupling method to fit extensive far-infrared vibration rotation tunneling (FIR–VRT) spectra of the Ar–HCl complex to a detailed two-dimensional potential surface with impressive success. More recently, two of us (R.C.C. and R.J.S.)[2] used the collocation method to accurately treat the dynamics in the three-dimensional Ar–H_2O complex, and were able to extract a detailed 3D potential surface by directly fitting the FIR–VRT data measured for the complex. It is, of course, of considerable interest to explore extensions of this rigorous approach with respect to computational feasability. The Ar–NH_3 complex is intrinsically a four-dimensional system, if the inversion coordinate is explicitly included in the large-amplitude Hamiltonian, and the same approach employed for the Ar–H_2O complex (fitting FIR–VRT spectra to a multidimensional PES using the collocation method for treating the dynamics) is currently being pursued by this group. In the present paper, however, we present the results of an analysis of FIR–VRT spectra of Ar–NH_3 with an intermediate level of sophistication, viz. with approximate separation of angular-radial coupling. This method, recently applied to the Ar–H_2O complex by Hutson,[3] involves fitting the observed FIR bending vibrations to an effective angular PES, and has been called "the reversed adiabatic approximation." Since this approach is straightforward to generalize to complexes of higher dimensionality [e.g., $(H_2O)_2$, a six-dimensional system], wherein the rigorous dynamical methods become prohibitive, it is worthwhile to further explore its attributes and limitations.

The chemical motivation for this study is the need to understand the "anomolous" weak bonding properties of ammonia, namely that there is no known example of NH_3 acting as a hydrogen bond donor in the gas phase, in spite of prevailing conventional wisdom. More explicitly, NH_3-containing complexes that have been studied by high resolution spectroscopy in the gas phase include NH_3–CF_3H,[4] NH_3–CO,[5] NH_3–CO_2,[6] NH_3–HCCH,[7] NH_3–HCN,[8] NH_3–HF,[9] NH_3–H_2O,[10] NH_3–N_2,[5] NH_3–N_2O,[11] NH_3–NH_3,[12,13] and Ar–NH_3,[14–16] and in no instance do the measured angular expectation values or vibrationally averaged structures indicate that NH_3 acts as a donor, although it is always an excellent acceptor. Ar–NH_3 is a good choice for initiating a systematic investigation of the weak bonding properties of NH_3, since Ar has no permanent electrical moments, its polarizability is known, and it can be treated as a point mass. It will thus serve as a structureless probe of the weak bonding properties of the ammonia monomer. Previous experimental work along these lines includes molecular beam scattering studies [He + NH_3 (Ref. 17)], as well as high resolution spectroscopic studies. [Ar–NH_3 (Refs. 14–16)]. There have also been several *ab initio* efforts directed towards rare gas–NH_3 complexes.[18–20]

A review of the salient features of the rotation–inversion

spectrum of the NH_3 monomer in its ground vibrational state[21] will facilitate a description of the spectrum of Ar–NH_3, since the NH_3 monomer exhibits only slightly hindered rotations within the complex. Ammonia is an oblate symmetric top belonging to the permutation-inversion molecular symmetry group $D_{3h}(M)$,[22] which is isomorphic with the D_{3h} point group. The three equivalent H nuclei (spin-1/2) result in two distinct spin manifolds, one of A symmetry ($I_{tot} = 3/2$), and one of E symmetry ($I_{tot} = 1/2$), which are accompanied by the strict rule for electric dipole transitions $A \leftrightarrow E$. The A states are the levels with $k \pmod 3 = 0$, where k is the projection of the angular momentum on the symmetry axis, and the E states are those with $k \pmod 3 \neq 0$. The $j = 0$, $k = 0$ state is the lowest state of A symmetry; $j = 1$, $k = 1$ is the lowest state of E symmetry. Both will have significant population in a 5–10 K supersonic expansion, since it is dipole forbidden for an E state to collisionally relax to an A state. The inversion tunneling, which mandates use of the $D_{3h}(M)$ molecular symmetry group, splits all levels into symmetric and antisymmetric pairs separated by ~24 GHz. In states with $k = 0$, only the symmetric levels are allowed for odd j, while only the antisymmetric levels are allowed for even j. Figure 1 shows the NH_3 energy levels and the dipole allowed $\Delta k = 0$, $\Delta j = 1$ transitions.

The Ar–NH_3 complex was first studied by microwave-IR double resonance.[14] That work established the existence of the complex, determined its binding energy to be less than 990 cm^{-1}, and estimated the rotational constant to be about 2.5 GHz. Later, the A-type microwave transitions[15] were assigned, which yielded the ground state dipole moment and rotational, centrifugal distortion, and quadrupole coupling constants, as well as proof that this state has A symmetry. Also measured in that work were some very irregular progressions, which were attributed, but not explicitly assigned, to the E states. The A or E symmetry of an Ar–NH_3 state is established by the symmetry of the free rotor state of NH_3 that it correlates to. The E states of Ar–NH_3 are expected to give rise to very complex spectra because both inversional levels are allowed and are strongly mixed by Coriolis interaction.

More recently, the $\Sigma(1_0,n=0) \leftarrow \Sigma(0_0,n=0)$ vibration–rotation band was measured in the FIR,[16] and Howard and co-workers have measured the mid-IR diode laser spectrum near the ν_2 umbrella vibration of the monomer, observing combination bands with the van der Waals modes.[23] In the present work, we report the measurement of two additional A state bands and the unambiguous assignment of all three. The FIR spectra in combination with the microwave data of Nelson *et al.*[15] are then analyzed to determine the effective angular PES sampled by Ar–NH_3 in its lowest stretching state. Currently, the E states are being investigated by Zwart and co-workers,[24] and their results will provide significant information about the inversion tunneling within the complex.

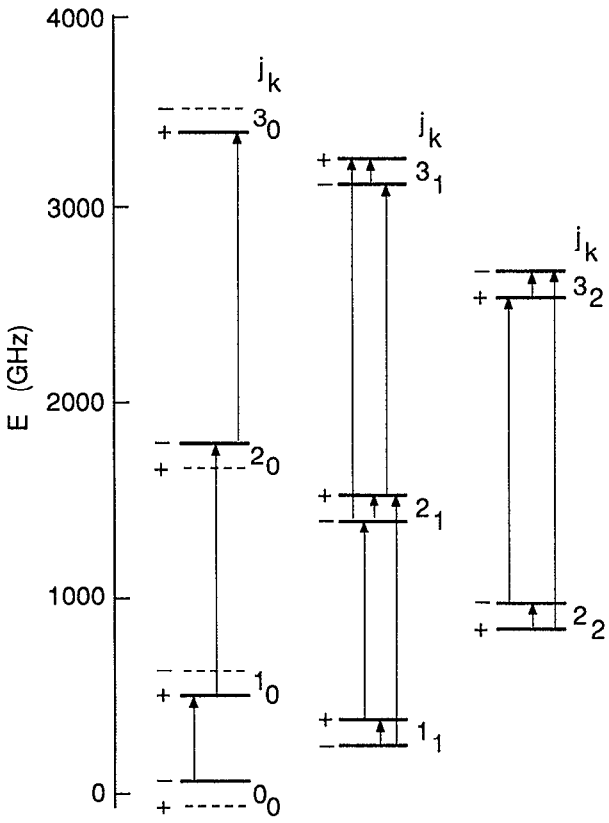

FIG. 1. Rotational energy levels and allowed transitions of free NH_3. The selection rules are $\Delta j = 0, \pm 1$ $\Delta k = 0$ ($\Delta j \neq 0$ when $k = 0$), and $+ \leftrightarrow -$.

II. EXPERIMENTAL

The Berkeley tunable far infrared laser spectrometer is described in detail in a forthcoming review,[25] and only a brief overview will be given here. Fixed frequency FIR radiation is generated by cw optical pumping of a 2.4 m far infrared molecular gas laser with a commercial (Apollo Lasers) 150 W line-tunable CO_2 laser. Far infrared radiation in the range 13 to 150 cm^{-1} has been generated with this system. The fixed frequency FIR radiation is mixed with tunable microwave radiation in a Schottky barrier diode (University of Virginia 117) to generate sum and difference frequencies at $\nu_{FIR} \pm n\nu_{MW}$, where $n = 1,2,3,\ldots$. Microwave power from 2 to 110 GHz is available, providing tunability of more than 7 cm^{-1} about each fixed-frequency FIR laser line. The tunable sideband power (10 to 100 μW) is separated from the much stronger (10 to 50 mW) carrier frequency (ν_{FIR}) with a polarizing Michelson interferometer, and the tunable sideband radiation is detected by an InSb detector.

The FIR laser frequencies used in this study were 527.9260 GHz (DCOOD), 584.3882 GHz (HCOOH), 980.5916 GHz (CH_3OD), 1016.8972 GHz (CH_3OD), and 1042.1504 GHz (CH_2F_2). The gas composition was established by employing a flow controller for each of the Ar and NH_3 gases. Typically, a 1% to 3% mixture of NH_3 in Ar was expanded through a 25 μm wide by 6 cm long slit orifice into a chamber pumped by a Roots blower (1200 cfm). Pressures of 500 to 800 torr of the mixture were maintained behind the nozzle, leading to a chamber pressure of 100 to 200 mtorr. The strongest signals observed exhibit signal to noise ratios of 800:1, and correspond to a fractional absorption of approximately 0.7%.

III. ANALYSIS

A. Vibrational assignment

Eigenstates of the Ar–NH_3 complex are classified according to the molecular symmetry group $D_{3h}(M)$.[22] The vibrational energy levels for the A_2 states of the complex and their correlation to the $k = 0$ energy levels of the NH_3 monomer (A states) are shown in Fig. 2. The notation used employs a capital Greek letter specifying the vibrational angular momentum of the complex [alternatively, it is the projection of the total angular momentum (J) of the complex on the van der Waals bond axis], followed by the usual j and k quantum numbers of the monomer that the particular level correlates with, and finally, the number of quanta (n) excited in the van der Waals stretch. For example $\Pi(1_0, n = 0)$ describes the state that correlates to the 1_0 level of free NH_3; it has one unit of angular momentum projected on the van der Waals bond axis, and no quanta of the van der Waals stretch excited.

The measured VRT transition frequencies for the three FIR bands observed are given in Table I. A stick spectrum of these three bands, with intensities calculated for 5 K is shown in Fig. 3. Initially, individual nonlinear least squares fits were performed separately for each band; it was found that in all three cases, the lower state had the same rotation (within one sigma) and distortion (within three sigma) constants as the ground state characterized in the microwave study of Nelson *et al.*[15] These three bands were assigned as the two lowest bending vibrations and the lowest stretching

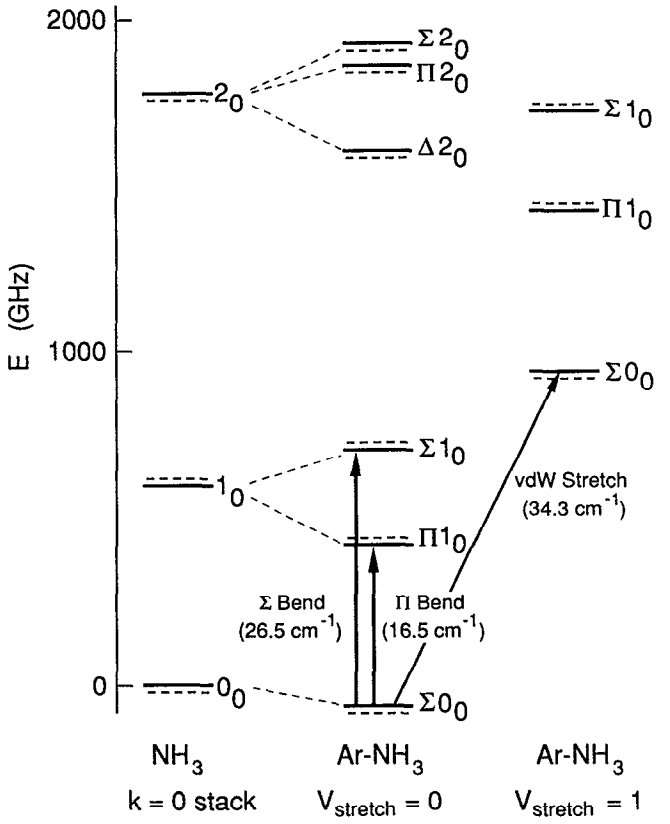

FIG. 2. Energy levels and observed vibrational transitions of Ar–NH_3 and their correlation to free NH_3 levels. Only states of NH_3 with $k = 0$ are shown.

TABLE I. Observed transitions and assignment. Residuals are from the least squares fit reported in Table II.

J'	J''	Freq (MHz)	O–C (MHz)
		Microwave transitions (Ref. 18)[a]	
2	1	11 504.559	0.00
3	2	17 251.513	0.01
		van der Waals stretch	
16	15	1 064 812.0	0.68
15	14	1 065 776.3	−1.08
14	13	1 066 305.1	−0.61
13	12	1 066 396.4	0.58
12	11	1 066 049.5	0.97
11	10	1 065 266.2	0.54
10	9	1 064 050.1	0.29
9	8	1 062 404.2	0.16
8	7	1 060 332.8	0.99
7	6	1 057 838.2	1.44
6	5	1 054 922.4	−0.21
5	4	1 051 592.8	−0.26
4	3	1 047 851.8	0.06
3	2	1 043 702.4	0.33
2	1	1 039 147.3	0.01
1	0	1 034 190.1	−0.26
0	1	1 023 080.6	−0.09
1	2	1 016 932.6	0.13
2	3	1 010 391.4	0.20
3	4	1 003 458.9	0.45
4	5	996 135.3	−0.23
5	6	988 423.4	−0.17
6	7	980 322.8	−0.72
7	8	971 835.6	−0.65
8	9	962 962.1	−0.51
9	10	953 702.6	−0.92
10	11	944 059.0	−1.10
		Sigma bend (Ref. 19)	
14	15	696 307.0	−0.95
13	14	703 581.0	1.47
12	13	710 717.0	0.53
11	12	717 728.5	0.19
10	11	724 623.0	0.33
9	10	731 405.0	−0.44
8	9	738 080.5	−0.57
7	8	744 653.3	0.61
5	6	757 492.3	1.13
4	5	763 758.7	−0.83
3	4	769 926.4	−0.79
2	3	775 992.7	−0.69
1	2	781 957.7	0.76
0	1	787 816.4	0.10
1	0	799 215.0	0.16
2	1	804 748.7	−0.77
3	2	810 170.0	−0.81
4	3	815 476.5	0.76
5	4	820 661.7	1.03
6	5	825 722.9	1.47
7	6	830 652.9	−0.29
9	8	840 105.1	−0.85
10	9	844 610.8	−1.55
		Pi bend	
15	14	559 119.0	0.12
13	12	552 422.3	−0.46
12	11	548 802.2	0.31
11	10	545 002.2	−0.21
10	9	541 027.0	0.25
9	8	536 877.3	0.08
8	7	532 556.0	−0.23
7	6	528 067.4	1.17
6	5	523 409.0	−0.66
5	4	518 588.5	−0.58
4	3	513 607.0	0.01
3	2	508 465.5	−0.37
2	1	503 167.9	−0.29

TABLE I. (*continued*).

J'	J''	Freq (MHz)	O–C (MHz)
1	0	497 717.1	0.74
1	1	492 140.6	0.19
2	2	492 196.0	0.05
3	3	492 279.5	0.14
4	4	492 390.8	0.06
5	5	492 530.2	−0.03
6	6	492 698.1	0.05
7	7	492 894.4	0.01
8	8	493 119.2	−0.34
9	9	493 373.4	−0.46
10	10	493 657.2	−0.50
11	11	493 972.0	0.46
12	12	494 316.2	0.33
13	13	494 691.6	0.32
14	14	495 098.6	0.17
15	15	495 538.1	0.02
16	16	496 011.0	−0.07
17	17	496 518.1	−0.26
18	18	497 060.9	−0.10
19	19	497 640.1	−0.08
20	20	498 257.4	0.18

[a] Microwave frequencies are the "origin" of the measured hyperfine multiplet.

vibration that occur among the A states, as indicated in Fig. 2. Since the relative energies of the $\Pi(1_0,n=0)$, $\Sigma(1_0,n=0)$, and $\Sigma(0_0,n=1)$ levels are not known *a priori*, details of the assignment follow. As only one band has a Q branch, its upper state must be the $\Pi(1_0,n=0)$. Distinguishing between the two $\Sigma\leftarrow\Sigma$ bands is possible because they have very different vibrational frequencies. The van der Waals stretching frequency is estimated to be 34.6 cm^{-1} from the pseudodiatomic ground state rotational and distortion constants using

$$\nu_s = \sqrt{\frac{4B^3}{D_J}}. \tag{1}$$

Moreover, any reasonable PES that calculates the Π bend to be near 16.5 cm^{-1} will place the Σ bend much closer to 26 cm^{-1} than 34 cm^{-1}. We accordingly assign the 34 cm^{-1} band as the van der Waals stretch and the 26.5 cm^{-1} band as the Σ bend. We have ruled out assignments to any of the E states, since $A\rightarrow E$ transitions are spin-forbidden and we know that the lower state of all three bands is the ground state, which has A symmetry. This assignment is consistent with the combination band assignments of Howard and coworkers for the $\nu_2=1$ state of the monomer.[23]

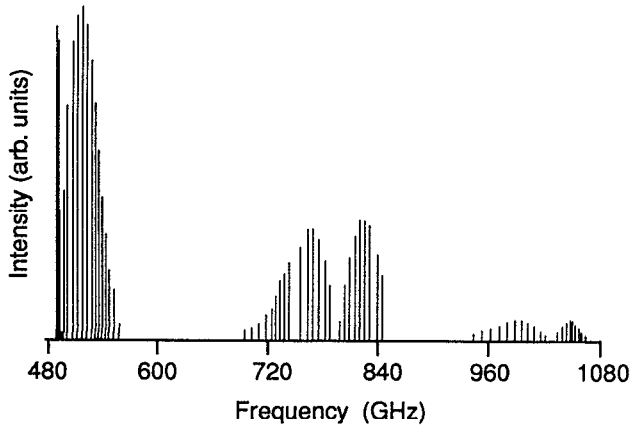

FIG. 3. Stick spectrum of the VRT bands of Ar–NH_3 reported in Table I. The vibrational band intensity is estimated by calculating the transition dipole using Eq. (22), and the rotational intensity is calculated for a 5 K temperature.

After establishing the assignment, we searched for, but did not find, the $\overline{\Sigma(0_0,n=1)}\leftarrow\Pi(1_0,n=0)$ hot band transitions. State designations with bars describe measured states that are coupled through the angular-radial interaction, and those without bars describe basis states. These designations will be used when it is necessary to distinguish between a measured (mixed) state and a basis state. The $\Pi(1_0,n=0)$ state is 16.6 cm^{-1} above the ground state and will have only $\sim 1\%$ as much population at 5 K. This transition dipole is also estimated to be much smaller than those for the bands measured. As discussed in Sec. IV, the measured $\overline{\Sigma(0_0,n=1)}$ state has approximately 30% $\Sigma(1_0,n=0)$ character and 70% $\Sigma(0_0,n=1)$ character. The $\overline{\Sigma(0_0n=1)}\leftarrow\Pi(1_0,n=0)$ transition dipole will thus be 30% of that for $\Sigma(1_0,n=0)\leftarrow\Pi(1_0,n=0)$, which itself is estimated to be 6 times smaller than that for $\Pi(1_0,n=0)\leftarrow\Sigma(0_0,n=0)$. The $\Sigma(0_0,n=1)\leftarrow\Pi(1_0,n=0)$ contribution to the transition dipole is calculated by differentiating Eq. (10) with respect to R and evaluating at $R=3.8290$ Å. This contribution will be exceedingly small as $d\mu/dR$ is only -0.015 D/Å. The 800:1 signal to noise ratio measured in the Π bend can be scaled to account for the lower population in the excited state and the reduced transition moment. This yields an estimated signal strength 60 times weaker than the noise level, thus making the hot band transitions far too weak to detect.

B. Hyperfine analysis

The quadrupole hyperfine constants of the complex were determined by fitting the hyperfine components of individual rovibrational transitions to the following parity adapted energy level expressions:[26]

$\Omega=0$ (Σ states),

$$E = -eqQ_{aa}f(I,J,F); \tag{2}$$

$\Omega=1$ ($\Pi^{\pm}$ state),

$$E_{\pm} = \left[eqQ_{aa}\left(\frac{3\Omega^2}{J(J+1)}-1\right) \pm \tfrac{1}{2}(eqQ_{bb}-eqQ_{cc})\right]f(I,J,F); \tag{3}$$

$$f(I,J,F) = \frac{(3/4)C(C+1)-I(I+1)J(J+1)}{2I(2I-1)(2J-1)(2J+3)};$$

$$C = F(F+1)-I(I+1)-J(J+1).$$

In the $\Pi^{\pm}$ state, the plus sign is used for the higher energy component of the parity doublet, and minus for the lower component. The ground state eqQ_{aa} was held fixed at the value 0.350 MHz, as obtained by Nelson *et al.*[15] since the microwave data has much higher resolution and precision

than the FIR data. For analysis of hyperfine structure in the $\Pi(1_0,n=0)$ state it is necessary to simultaneously fit two transitions, since these patterns are determined by two unknown parameters. We chose to simultaneously fit $R(n)$ and $Q(n+1)$ pairs.

For most of the transitions, the quadrupole multiplet was not fully resolved; therefore a least squares fit of the multiplet line shape was carried out. The determinable parameters are the line center, the FWHM, the quadrupole coupling constants, the modulation index, and base line and vertical scaling parameters. Lorentzian line shapes were employed for the unmodulated lines, rather than Gaussians, because the optimal FWHM was 670 kHz at 1030 GHz and 600 kHz at 530 GHz. If the spectral lines were Doppler broadened (Gaussian), the FWHM would scale linearly with absorption frequency. Also, it was found that the standard deviation of the fit was over two times better when using Lorentzian rather than Gaussian line shapes. Of course, Voigt line shapes would ultimately give the best fit, but at the expense of introducing an additional parameter in the fit and thus increasing the problems with parameter correlations. Figure 4 compares the calculated and experimental line shapes for the simultaneous fit of the $Q(2)$ and $R(1)$ lines of the Π bending transition.

The quadrupole coupling constants obtained for each state are given in Table II. In the Σ states only eqQ_{aa} is measurable, and this is the quantity reported in Table II. In the Π state, both eqQ_{aa} and the difference $(eqQ_{bb}-eqQ_{cc})$ are determinable. Since LaPlace's equation always holds, we have the additional constraint that $eqQ_{aa}+eqQ_{bb}+eqQ_{cc}=0$; hence, for the Π state we report values for all three quadrupole coupling constants. The given uncertainties reflect the spread of values obtained when the average is computed from measurements of several J states. The uncertainty in the quadrupole coupling constant calculated for any given J is actually about 10 times smaller than these quoted values, but we choose not to assert that the quadrupole coupling constant is different for each J for two reasons. First, there is some uncertainty in the model used to fit the line shapes; specifically, the FWHM is not precisely known, and the modulation depth is only known to about 5%. Secondly, the ground state eqQ_{aa} was fixed at the value reported by Nelson *et al.*[15] and was assumed to be independent of J.

We estimate the experimental uncertainties in the quadrupole coupling constants to be larger than the effects of induction on the hyperfine structure. Thus, the following relations among the quadrupole coupling constants of the complex and that of the monomer are assumed to be valid:[27]

$$eqQ_{aa}=eqQ_{NH_3}\langle P_2(\cos\theta)\rangle, \tag{4}$$

$$eqQ_{bb}-eqQ_{cc}=eqQ_{NH_3}[1-\langle P_2(\cos\theta)\rangle], \tag{5}$$

and upon rearrangement,

$$eqQ_{aa}+eqQ_{bb}-eqQ_{cc}=eqQ_{NH_3}. \tag{6}$$

The quadrupole coupling constant of the NH_3 monomer in the $\Pi(1_0,n=0)$ state of Ar–NH_3 is determined to be $-4.17(9)$ MHz, using Eq. (6) and the measured values for the quadrupole coupling constants of the complex in this state from Table II. Free NH_3 has a quadrupole coupling constant of $-4.089\,83(2)$ MHz.[28] The fact that both free and complexed NH_3 have essentially the same quadrupole coupling constant indicates that the electric field gradient at the N nucleus is unchanged upon complexation, which implies, in turn, that the structure of the NH_3 subunit in the $\Pi(1_0,n=0)$ state of Ar–NH_3 is unchanged upon complexation. However, one can not unequivocally conclude that the inversion motion is unaffected upon complexation, because the electric field gradient at the N nucleus is the same for either of the symmetric pyramidal structures. Thus, the rate at which it interchanges, if it does so at all, will not affect the effective quadrupole coupling constant. What *is* implied by the above results, is that if the inversion is slowed or quenched, the complexed NH_3 in the $\Pi(1_0,n=0)$ state retains the same bond lengths and bond angles as free NH_3 in either minimum of the double-well potential.

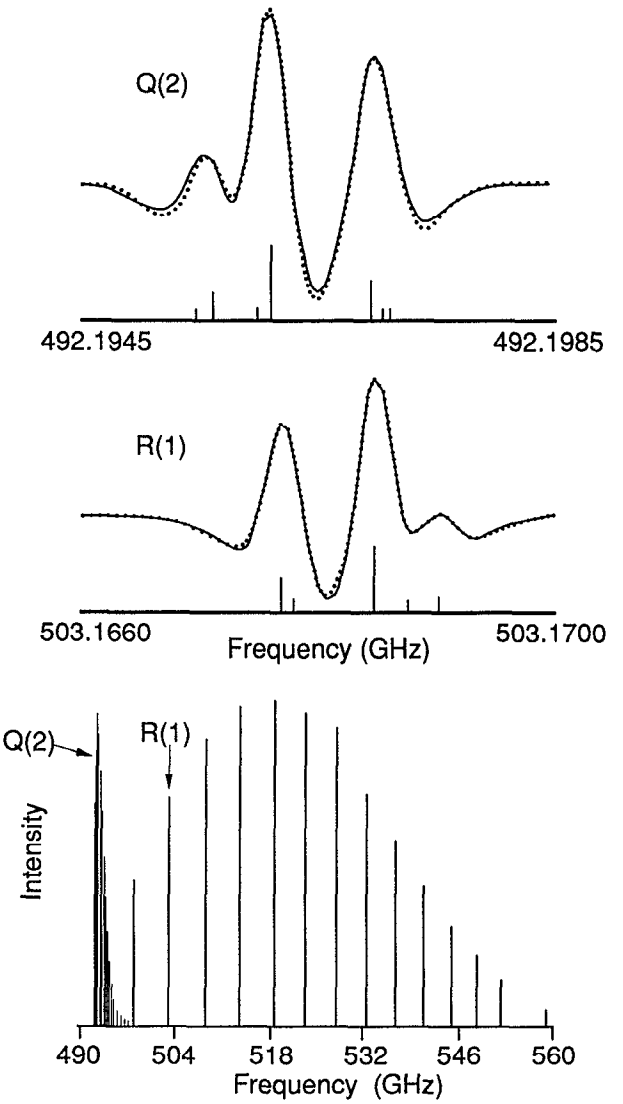

FIG. 4. Bottom: Stick spectrum of the Q and R branches of the $\Pi(1_0,n=0)\leftarrow\Sigma(0_0,n=0)$ band. The P branch transitions occur at too low frequency to be measured. Top: Comparison of calculated and experimental line shapes for the $Q(2)$ and $R(1)$ transitions. Below each partially resolved multiplet is its stick spectrum.

TABLE II. Molecular constants obtained from simultaneous nonlinear least squares fit. Uncertainties in parentheses are 1σ. The standard deviation of the fit is 0.625 MHz.

State	$\Sigma(0_0,n=0)$	$\Pi^+(1_0,n=0)$	$\Pi^-(1_0,n=0)$	$\Sigma(1_0,n=0)$	$\Sigma(0_0,n=1)$
ν_0 (GHz)		495.0033(3)		793.5696(6)	1028.8340(3)
B (MHz)	2876.847(1)	2890.548(9)		2752.09(2)	2660.41(1)
D (kHz)	88.4(1)	86.9(1)	75.9(2)	106.6(3)	110.8(2)
H (Hz)	−87(8)	−80(8)	103(8)	−438(14)	−21(7)
β (MHz)			5563.7(5)		
Fractional "$\Sigma(1_0,n=0)$" character				0.6886	0.3114
eqQ_{aa} (MHz)	0.350(8)[a]	0.92(6)		−0.84(1)	−0.19(5)
eqQ_{bb} (MHz)		−3.01(5)			
eqQ_{cc} (MHz)		2.09(5)			

[a] Reference 15.

IV. DEPERTURBATION: CORIOLIS MIXING AND ANGULAR-RADIAL COUPLING

In proceeding from the vibrational assignment given in Sec. III A to the determination of the angular potential surface for the complex, it was realized that a strong mixing existed among the three excited intermolecular vibrational states observed here, and that the observables must be corrected for these perturbations before a potential surface could be determined from them. There is a Coriolis interaction between the $\Sigma(1_0,n=0)$ state and the $\Pi^-(1_0,n=0)$ levels, and a strong angular-radial coupling between the $\Sigma(1_0,n=0)$ and $\Sigma(0_0,n=1)$ states, as previously alluded to. The Coriolis interaction between $\Pi^-(1_0,n=0)$ and $\Sigma(1_0,n=0)$ is thus distributed over both the $\overline{\Sigma(1_0n=0)}$ and $\overline{\Sigma(0_0,n=1)}$ states. The angular-radial mixing coefficients, C_{BB} and C_{BS}, are determined from the measured quadrupole coupling constants of the $\Sigma(0_0,n=0)$, $\overline{\Sigma(1_0,n=0)}$, and $\overline{\Sigma(0_0,n=1)}$ states, as discussed below, and are fixed at 0.8298 and 0.5580, respectively. The values of $(C_{BB})^2$ and $(C_{BS})^2$ may be interpreted as the fraction of $\Sigma(1_0,n=0)$ character contained in the states, i.e., the amount of the Σ bend basis state in the measured Σ bend and Σ stretch states, respectively. The Coriolis interaction energy of these states was obtained by diagonalizing the following matrix for each J:

$$\begin{bmatrix} E_J(\Pi^-) & \beta[J(J+1)C_{BB}]^{1/2} & \beta[J(J+1)C_{BS}]^{1/2} \\ \beta[J(J+1)C_{BB}]^{1/2} & E_J(\Sigma_{\text{bend}}) & 0 \\ \beta[J(J+1)C_{BS}]^{1/2} & 0 & E_J(\Sigma_{\text{stretch}}) \end{bmatrix}.$$

Here E_J is the energy of the Jth rotational level before interaction, as is obtained from Eqs. (8) and (9), and β is the Π bend–Σ bend Coriolis interaction parameter.

We then performed a simultaneous weighted nonlinear least squares fit of all the available microwave and FIR data, with weightings appropriate to the precision of each measurement. The energy level expressions used were

$$E_J = \nu_0 + BJ(J+1) - D[J(J+1)]^2 + H[J(J+1)]^3 \quad (8)$$

for the Σ states, and

$$E_J^+ = \nu_0 + B[J(J+1) - l^2] - D_\pm[J(J+1) - l^2]^2 + H_\pm[J(J+1) - l^2]^3 \quad (9)$$

for the Π state. The results of the simultaneous fit are given in Table II. The residuals reported in Table I are for this simultaneous fit, not for the individual fits that were initially performed.

Before fitting the available experimental observables (vibrational frequencies, rotational constants, quadrupole coupling constants) to an angular PES, it is necessary to correct them for the effects of the induced dipole moment and that of angular-radial coupling in the potential. In the multipole expansion,[29] the dipole moment of the complex is

$$\mu_a = \mu_{NH_3}\langle P_1(\cos\theta)\rangle + \alpha_{Ar}\left[\frac{2\mu_{NH_3}\langle P_1(\cos\theta)\rangle}{R^3} + \frac{3\Theta\langle P_2(\cos\theta)\rangle}{R^4}\right], \quad (10)$$

where the first term is the projection of the NH_3 monomer dipole moment on the van der Waals bond axis, and the second term is the multipole-induced dipole, with terms up to quadrupole-interaction retained. We have neglected the dipole induced in the NH_3 from the induced Ar dipole because it contributes only ca. 0.2% to the measured dipole. The dipole moment of the complex has been measured only in the ground state.[15] The constants used in Eq. (10) are $|\mu_a| = 0.2803(3)$ D,[15] $\mu_{NH_3} = 1.471\,49(15)$ D,[28] $\alpha_{Ar} = 1.6443$ Å^3,[30] $R = 3.8290$ Å, $\Theta = -2.32(7)$ D Å.[31] The value of $\langle P_2(\cos\theta)\rangle$ for the ground state is determined to be −0.086 from Eq. (4) and the measured eqQ_{aa}. Solving

Eq. (10) for $|\langle P_1(\cos\theta)\rangle|$ yields 0.1771; the quantity $\mu_{NH_3}|\langle P_1(\cos\theta)\rangle| = 0.2606$ D was fit rather than μ_a itself in the PES determination.

The angular-radial coupling between the $\Sigma(1_0,n=0)$ and $\Sigma(0_0,n=1)$ basis states mixes them in the uncoupled basis. If we let the uncoupled basis states be $|B\rangle$ and $|S\rangle$, for bend and stretch, the frequencies of the coupled vibrations will be the eigenvalues of the following matrix, and its eigenvectors will be the basis functions for the coupled states:

$$\begin{array}{c} \\ \langle B| \\ \langle S| \end{array} \begin{array}{c} \begin{array}{cc} |B\rangle & |S\rangle \end{array} \\ \begin{bmatrix} A & C \\ C & B \end{bmatrix} \end{array}. \tag{11}$$

Here A and B are the uncoupled frequencies, and C is responsible for mixing the two states.

The measured quadrupole coupling constants of the $\Sigma(0_0,n=0)$, $\overline{\Sigma(1_0,n=0)}$, and $\overline{\Sigma(0_0,n=1)}$ states allow the basis functions of the coupled Σ bend and Σ stretch to be determined. In the absence of angular-radial coupling, the $\Sigma(0_0,n=0)$ and $\overline{\Sigma(0_0,n=1)}$ states would have equal quadrupole coupling constants (0.350 MHz),[15] since in that case, the addition of one quantum of van der Waals stretch would not affect the orientational averaging of the NH_3 subunit. The measured values of eqQ_{aa} in the $\overline{\Sigma(1_0,n=0)}$ and $\overline{\Sigma(0_0,n=1)}$ states [$-0.842(13)$ MHz and $-0.189(52)$ MHz, respectively] can be expressed as linear combinations of their deperturbed values. The square root of the coefficients of these linear combinations are then the desired eigenvectors of the coupled basis wave functions in the uncoupled basis, i.e., the eigenvectors of Eq. (11). In particular, we have

$$\begin{aligned} &Q_B(C_{BB})^2 + 0.350(C_{BS})^2 = -0.842, \\ &Q_B(C_{SB})^2 + 0.350(C_{SS})^2 = -0.189, \\ &(C_{BB})^2 + (C_{BS})^2 = 1. \end{aligned} \tag{12}$$

Q_B is the deperturbed quadrupole coupling constant in the $\Sigma(1_0,n=0)$ state, 0.350 MHz is the deperturbed quadrupole coupling constant in the $\Sigma(0_0,n=1)$ state, and $(C_{BB})^2 = (C_{SS})^2$ and $(C_{BS})^2 = (C_{SB})^2$ because this analysis is based on a two state model described by a symmetric matrix. Solving Eqs. (12) yield $Q_B = -1.381(60)$ MHz, $(C_{BB})^2 = (C_{SS})^2 = 0.689(20)$, and $(C_{BS})^2 = (C_{SB})^2 = 0.311(20)$. Matrix (11) is now diagonalized with the constraints that the eigenvalues are the observed intermolecular vibrational frequencies (26.47 and 34.32 cm^{-1}) and the squared components of the eigenvectors are 0.689 and 0.311. The resulting deperturbed Σ bend and Σ stretch frequencies are 28.89(16) cm^{-1} and 31.85(17) cm^{-1}, and the off-diagonal mixing element is 3.63(7) cm^{-1}.

Another consequence of angular-radial coupling is that the van der Waals bond is considerably longer in the $\overline{\Sigma(1_0,n=0)}$ state than it would have been without the coupling. Since the separation of the $J=0$ and $J=1$ levels (essentially twice the rotational constant) will be directly affected by this, it is necessary to calculate the deperturbed values of these spacings before performing the fit of the PES. The measured 0 to 1 spacings are 5645.2 MHz and 5356.3 MHz for the $\overline{\Sigma(1_0,n=0)}$ and $\overline{\Sigma(0_0,n=1)}$ levels, respectively. The angular-radial mixing coefficients, $(C_{BB})^2$, $(C_{BS})^2$, $(C_{SB})^2$, and $(C_{SS})^2$ are all known, leaving two equations with two unknowns:

$$\begin{aligned} &S_B(C_{BB})^2 + S_S(C_{BS})^2 = 5645.2 \text{ MHz}, \\ &S_B(C_{SB})^2 + S_S(C_{SS})^2 = 5356.3 \text{ MHz}. \end{aligned} \tag{13}$$

S_B and S_S, the deperturbed $J=1\leftarrow0$ spacings in the Σ bend and Σ stretch are found to be 5883.6 MHz and 5117.9 MHz, respectively.

The third and final consequence of angular-radial coupling considered here is its effect on the inversion splitting, which we assume to be unaffected by complexation in the A states. Just as the $J=1\leftarrow0$ rotational level spacing is changed, so is the inversion spacing. The inversion splitting shifts the $\Sigma(1_0,n=0)$ state down by 0.397 cm^{-1} ($\sim$12 GHz) and the $\Sigma(0_0,n=1)$ state up by 0.397 cm^{-1} (see Fig. 2). The shift of the $\overline{\Sigma(1_0,n=0)}$ state is given by $(-0.397\ cm^{-1})(0.689) + (0.397\ cm^{-1})(0.311) = -0.150\ cm^{-1}$. To account for this, 0.247 cm^{-1} was added to the uncoupled Σ bending frequency, 28.89(16) cm^{-1}, to yield a final deperturbed bending frequency of 29.14(16) cm^{-1}.

V. POTENTIAL SURFACE DETERMINATION

Having assigned and analyzed the three A state bands of the complex, the effective Ar–NH_3 angular potential energy surface can then be determined by fitting the deperturbed bending vibrational frequencies, quadrupole coupling constants, ground state dipole moment, and the rotational constants. The ultimate goal of this work is to determine the full four-dimensional intermolecular potential surface $V(R,\theta,\chi,\rho)$, where R, θ, and χ are the Jacobi coordinates of the complex as indicated in Fig. 5, and ρ is the NH_3 inversion coordinate. We can restrict the treatment to $V(\theta,\chi)$ if we account for angular-radial coupling by using deperturbed observables and assume that the NH_3 subunit inversion is unchanged upon complexation. The assumption of unperturbed inversion will be justified by the fact that the center of mass separation in the free rotor limit (3.8290 Å) is quite large. Therefore, at least in states wherein the symmetry axis of NH_3 is localized to be roughly perpendicular to the van

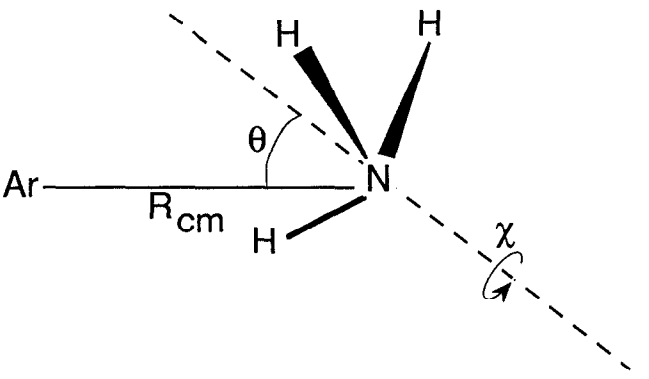

FIG. 5. Coordinate system used for Ar–NH_3. $R_{c.m.}$ is the center of mass separation of the Ar and the NH_3. θ is the angle between $\hat{r}$ (the NH_3 symmetry axis) and $\hat{R}$, and χ is the rotation of the NH_3 about its symmetry axis.

der Waals bond, the Ar should not significantly affect the NH_3 inversion potential. Evidence for nearly free inversion in some of the E states has been presented by Fraser *et al.*,[14] and we also find what can be interpreted to be free inversion in the $\Pi(1_0,n=0)$ state. The nature of the inversion motion can be treated more rigorously in spectra arising from the E states, since both symmetric and antisymmetric inversion levels are allowed when $k>0$.

A parameterization of the angular PES analogous to that developed for Ar–H_2O by Hutson[3] has been carried out for Ar–NH_3. This method is based on the hindered rotation of the polyatomic subunit in the complex. A brief description of the method is presented, but the interested reader is directed to Ref. 3 for a more complete discussion. The potential energy of the complex is expressed as an expansion in spherical harmonics, and the resulting energy levels, dipole moments, quadrupole coupling constants, and the change in rotational constant due to orientation effects are calculated. This model is incorporated in a nonlinear least squares fitting routine to determine the coefficients of the angular PES.

The effective angular Hamiltonian is

$$\hat{H}=\frac{\hbar^2}{2\mu R^2}(\hat{J}^2+\hat{j}^2-2\hat{J}\cdot\hat{j})+\hat{H}_{\rm mon}+V(\theta,\chi), \tag{14}$$

where the first term describes the end-over-end rotation of the complex, with μ being the collisional reduced mass of the complex and R the center of mass separation of the Ar and NH_3, $\hat{J}$ is the total angular momentum of the system, $\hat{j}$ is the internal angular momentum of the monomer, $\hat{H}_{\rm mon}$ is the Hamiltonian of the molecular monomer, and $V(\theta,\chi)$ is the intermolecular bending potential, which is taken to be average over the zero-point vibrations of the monomer. Ignoring the inversion motion, the molecular monomer Hamiltonian is simply

$$\hat{H}_{\rm mon}=B_x\hat{j}_x^2+B_y\hat{j}_y^2+B_z\hat{j}_z^2, \tag{15}$$

where $\hat{j}_x$, $\hat{j}_y$, and $\hat{j}_z$ are the angular momentum operators in the Cartesian frame of the monomer. The total wavefunction is expanded in terms of body-fixed angular functions

$$\Phi_{jkM}^{JM}(\hat{R},\hat{r})=D_{M\Omega}^{J*}(\alpha,\beta,0)D_{\Omega k}^{j}(\phi,\theta,\chi), \tag{16}$$

where $D_{M\Omega}^{J*}(\alpha,\beta,0)$ is a rotation matrix with $[(2J+1)/4\pi]^{1/2}$ normalization describing the orientation of the $\hat{R}$ vector in space, and $D_{\Omega k}^{j}(\phi,\theta,\chi)$ is a rotation matrix with $[(2j+1)/8\pi^2]^{1/2}$ normalization describing the orientation of the monomer in the body-fixed axis system. $\hat{R}$ is the unit vector pointing from the center of mass of the NH_3 to the Ar atom, and $\hat{r}$ is the unit vector along the symmetry axis of NH_3, pointing from N to the plane of the hydrogens. The quantum numbers that describe all the angular degrees of freedom are then j, k, J, Ω, M, where j quantizes the angular momentum of the NH_3 subunit, k is its projection on the NH_3 symmetry axis, J quantizes the total angular momentum of the complex, Ω is the projection of J on the van der Waals bond axis, and M is the spaced fixed projection of J. In these coordinates, the interaction potential is independent of J and diagonal in Ω, although it still couples states with different j.

The nonzero matrix elements of $(\hbar^2/2\mu R^2)(\hat{J}^2+\hat{j}^2-2\hat{J}\cdot\hat{j})$ are given by

$$\begin{aligned}(jk\Omega J|(\hbar^2/2\mu R^2)(\hat{J}^2+\hat{j}^2-2\hat{J}\cdot\hat{j})|j'k'\Omega'J')&=(1/2\mu R^2)[J(J+1)+j(j+1)-2\Omega^2]\delta_{jj'}\delta_{kk'}\delta_{\Omega\Omega'}\delta_{JJ'}\\&+(1/2\mu R^2)[J(J+1)-\Omega(\Omega\pm1)]^{1/2}\\&\times[j(j+1)-\Omega(\Omega\pm1)]^{1/2}\delta_{jj'}\delta_{kk'}\delta_{\Omega\pm1\Omega'}\delta_{JJ'},\end{aligned} \tag{17}$$

where the round brackets ( ) indicate integration over all coordinates except R.

The nonzero matrix elements for $\hat{H}_{\rm mon}$ are

$$\begin{aligned}(jk\Omega J|\hat{H}_{\rm mon}|j'k'\Omega'J')&=\{\tfrac{1}{2}(A+B)[j(j+1)-k^2]+Ck^2\}\delta_{jj'}\delta_{kk'}\delta_{\Omega\Omega'}\delta_{JJ'},\end{aligned} \tag{18}$$

where $A=B=9.944\ 11\ {\rm cm}^{-1}$, and $C=6.228\ 52\ {\rm cm}^{-1}$ are the rotational constants of NH_3.[32]

The potential energy is expanded in renormalized spherical harmonics $C_{\lambda\mu}(\theta,\chi)$:

$$V(R,\theta,\chi)=\sum_{\lambda\mu}V_{\lambda\mu}(R)C_{\lambda\mu}(\theta,\chi). \tag{19}$$

Here, $V_{\lambda\mu}=0$ if $\mu\ (\mathrm{mod}\ 3)\neq0$ due to the threefold symmetry of NH_3. Furthermore, $V_{\lambda-\mu}=(-1)^{\mu}V_{\lambda\mu}$ because the xz plane of NH_3 is a plane of symmetry

$$\begin{aligned}V(R,\theta,\chi)=\sum_{0\leqslant\mu\leqslant\lambda}V_{\lambda\mu}(R)[&C_{\lambda\mu}(\theta,\chi)\\&+(-1)^{\mu}C_{\lambda-\mu}(\theta,\chi)](1+\delta_{\mu0})^{-1}.\end{aligned} \tag{20}$$

We have considered the first four terms in this expansion, viz. V_{10}, V_{20}, V_{30}, V_{33}. The leading term (V_{00}) can be set to zero, since it is isotropic and has no effect on the spacings of the bending eigenstates. The matrix elements of the potential are

$$(jk\Omega J|V(R,\theta,\chi)|j'k'\Omega J)=\sum_{\lambda\mu}V_{\lambda\mu}(R)g_{\lambda\mu}(jkj'k'\Omega). \tag{21}$$

The Gaunt coupling coefficients $g_{\lambda\mu}(jkj'k'\Omega)$ are

$$\begin{aligned}g_{\lambda\mu}(jkj'k'\Omega)&\equiv(jk\Omega J|C_{\lambda\mu}(\theta,\chi)|j'k'\Omega J)\\&=(-1)^{\Omega-k}[(2j+1)(2j'+1)]^{1/2}\\&\times\begin{pmatrix}j&\lambda&j'\\-k&\mu&k'\end{pmatrix}\begin{pmatrix}j&\lambda&j'\\-\Omega&0&\Omega\end{pmatrix}.\end{aligned} \tag{22}$$

In this study, energy level patterns were calculated for $J=0$, 1, and 2. For each value of J, the ranges of Ω, j, and k that make up the basis states are given by $-J\leqslant\Omega\leqslant J$, $|\Omega|\leqslant j\leqslant7$, and $-j\leqslant k\leqslant j$ (k is restricted to 0, ±3, ±6,... since only the A states are relevant here). This provided nonmonotonic convergence to approximately $0.01\ {\rm cm}^{-1}$ for the vibrational frequencies, and better than 0.1 MHz convergence for the rotational term values. The intermolecular vibrational energy levels are the eigenvalues of this diagonalization for a given J. The expectation values of $P_1(\cos\theta)$, required for interpretation of the dipole moments of weakly bound complexes, are obtained by calculating the expectation value of the expression

$$\sum_{\Omega=-1}^{1}(-1)^{\Omega_i-k_i}[(2j_i+1)(2j_f+1)]^{1/2}\times\begin{pmatrix} j_i & 1 & j_f\\ -k_i & 0 & k_f\end{pmatrix}\begin{pmatrix} j_i & 1 & j_f\\ -\Omega_i & \Omega & \Omega_f\end{pmatrix} \quad (23)$$

over the eigenvector for the state of interest. Similarly, $\langle P_2(\cos\theta)\rangle$ are used to determine the axial quadrupole coupling constants of the complex, and are obtained by changing the 1 to 2 in the 3-j symbols in the equation above and including only $\Omega=0$. The nonaxial quadrupole coupling constants, observable in states with vibrational angular momentum, are obtained through Eq. (6) along with the axial term.

Table III contains the quantities fit, the relative weights used, and the results of the fit. The relative weights used represent the combined effects of the absolute magnitude of the quantity, the experimental uncertainty, and an estimate of the uncertainty in the model. The sign of V_{10} can not be determined because the sign of μ_a has not been determined experimentally.[15] We arbitrarily constrain V_{10} to be positive. This choice of sign causes the dipole moment of the complex to be negative, and consequently $\langle\theta\rangle$ to be $>90°$. The Ar–NH_3 complex is undergoing such large amplitude motions that $\langle\theta\rangle$ should *not* be interpreted as the "average" angle between the NH_3 symmetry axis and the van der Waals bond. The sign of V_{20} determines the relative ordering of the $\Sigma(1_0,n=0)$ and $\Pi(1_0,n=0)$ levels, and therefore can be deduced from the experimental data. V_{30} could not be fit independently because it was too highly correlated with V_{10} and V_{20} for the fit to converge. Instead, a series of fits was carried out for a range of V_{30} as Hutson did in the Ar–H_2O study.[3] Figure 6 is a plot of V_{10} and V_{20} and the dimensionless root-mean-squared deviation[33] of the fits versus V_{30} for $-25\ \text{cm}^{-1}\leqslant V_{30}\leqslant 25\ \text{cm}^{-1}$. Over this range the RMSD of the fit only varies by a factor of 2, with its minimum occurring at $V_{30}=3\ \text{cm}^{-1}$.

Figure 7 is a plot of the potential surface expansion coefficients, energy levels, and squared wave functions vs θ for $0°\leqslant\theta\leqslant 180°$, obtained from the best fit [$V_{10}=10.48(27)\ \text{cm}^{-1}$, $V_{20}=20.79(21)\ \text{cm}^{-1}$, and $V_{30}=3\ \text{cm}^{-1}$], and from fits with $V_{30}=\pm 15\ \text{cm}^{-1}$ (V_{10} and V_{20} are the corresponding values plotted in Fig. 6). For reference, the same quantities are plotted for the completely isotropic potential. If V_{10} had been chosen to be negative, the horizontal axis would run from 180° to 0° (rather than 0° to 180°, as plotted).

The information needed to determine V_{30} and V_{33} will be obtained when transitions involving levels with $k=1$ (E states) are measured and analyzed. The energy levels of the $\Pi(2_1,n=0)$ and $\Sigma(1_1,n=0)$ states will be very sensitive to V_{30}, as is evident from the 3-j symbols in Eq. (21). The wave functions, and therefore dipole moments, quadrupole coupling constants, and intensities will also be sensitive to V_{30}. There are two strong $\Pi(2_1,n=0)\leftarrow\Sigma(1_1,n=0)$ transitions, among others, and we predict that their transition energies will shift in opposite directions by about $10\ \text{cm}^{-1}$ over the range of V_{30} where the RMSD shown in Fig. 6 is essentially constant ($-15\ \text{cm}^{-1}\leqslant V_{30}\leqslant 15\ \text{cm}^{-1}$). A nonzero V_{33} will manifest itself by allowing transitions with $\Delta k=1$ which are otherwise forbidden. For example, if V_{33} is $\sim 20\ \text{cm}^{-1}$ the transition dipole for $\Sigma,\Pi(2_2,n=0)\leftarrow\Sigma,\Pi(1_1,n=0)$ transitions will be only 2 to 3 times smaller than those for the more strongly allowed (and observable) $\Delta k=0$ transitions.

VI. DISCUSSION

The measurement and assignment of the three A state VRT transitions accessible in a cold supersonic expansion has been carried out. The mixing of these states by Coriolis and angular-radial coupling has been treated explicitly. The molecular constants obtained from a simultaneous least squares analysis have enabled the effective angular potential energy surface to be determined. Two assumptions were

TABLE III. Results of fit of potential energy surface.

Parameter	Value
V_{10}	$10.48(27)\ \text{cm}^{-1}$
V_{20}	$20.79(21)\ \text{cm}^{-1}$
V_{30}	$3.0\ \text{cm}^{-1}$ (fixed)
V_{33}	0.0 (fixed)
B_{complex}[a]	$0.096\,27(13)\ \text{cm}^{-1}$

Quantity	Weight	Observed	Calculated	Obs–Calc
Σ bend $R(0)$	3	$29.14\ \text{cm}^{-1}$	$29.08\ \text{cm}^{-1}$	$0.06\ \text{cm}^{-1}$
Π bend $R(0)$	5	$16.59\ \text{cm}^{-1}$	$16.68\ \text{cm}^{-1}$	$-0.09\ \text{cm}^{-1}$
$\Sigma(0_0,n=0)$ dipole	30	−0.261 D	−0.262 D	0.001 D
$\Sigma(0_0,n=0)\ eqQ_{aa}$	20	0.350 MHz	0.361 MHz	−0.011 MHz
$\Sigma(1_0,n=0)\ eqQ_{aa}$	3	−1.38 MHz	−1.25 MHz	−0.13 MHz
$\Pi(1_0,n=0)\ eqQ_{aa}$	5	0.92 MHz	0.95 MHz	−0.03 MHz
$\Sigma(0_0,n=0)$ "$2B$"[b]	500	$0.1919\ \text{cm}^{-1}$	$0.1924\ \text{cm}^{-1}$	$-0.0005\ \text{cm}^{-1}$
$\Sigma(1_0,n=0)$ "$2B$"[b]	300	$0.1963\ \text{cm}^{-1}$	$0.1983\ \text{cm}^{-1}$	$-0.0020\ \text{cm}^{-1}$
$\Pi(1_0,n=0)$ "$4B$"[b]	500	$0.3856\ \text{cm}^{-1}$	$0.3850\ \text{cm}^{-1}$	$0.0006\ \text{cm}^{-1}$
$\Pi(1_0,n=0)$ "$2q_l$"[b]	500	$0.0059\ \text{cm}^{-1}$	$0.0058\ \text{cm}^{-1}$	$-0.0001\ \text{cm}^{-1}$

[a] $R=3.8290$ Å (7.2359 a_0) from the relation: $B_{\text{complex}}=1/(2\mu R^2)$.

[b] "$2B$" is the $J=0\rightarrow 1$ spacing, "$4B$" is the $J=1\rightarrow 2$ spacing, and "$2q_l$" is splitting of $J=1$ in the Π state.

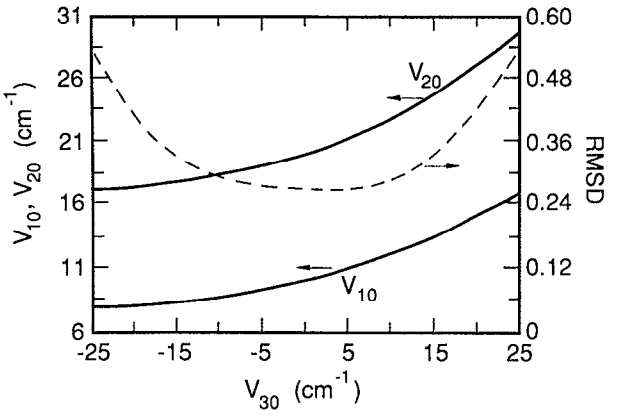

FIG. 6. V_{10} and V_{20} (solid lines) and the dimensionless root mean squared deviation (dashed line) of the fit as a function of V_{30} for -25 cm^{-1} $\leqslant V_{30} \leqslant 25$ cm^{-1}. The scale on the left is for V_{10} and V_{20}, and the scale on the right is for RMSD.

made. (1) All angular-radial coupling is accounted for in the deperturbation of the Σ bend and Σ stretch; (2) the NH_3 inversion potential is unaffected by complexation.

The fact that all the data (vibrational frequency, rotational constant, hyperfine parameter) from the $\Sigma(1_0,n=0)$ state could be included in the fit after decoupling the bend and stretch, whereas only the vibrational frequency could be fit prior to the decoupling, is strong evidence that the first assumption is justified, at least in the context of the present data set. The validity of the second assumption is harder to evaluate. Although one can infer from the hyperfine analysis that even if the inversion is slowed or quenched in the $\Pi(1_0,n=0)$ state, the structure of the NH_3 subunit remains unchanged, similar assertions regarding the $\Sigma(1_0,n=0)$ state cannot be made, since $\Omega=0$ in that case, and only eqQ_{aa} is experimentally observable. Here, Eq. (6) cannot be employed to estimate how much the NH_3 field gradient changes in this state. In fact, it can be seen from the wave functions in Fig. 7 that there will be a much greater likelihood that complexation will affect the NH_3 inversion potential in the $\Sigma(1_0,n=0)$ state than in the $\Pi(1_0,n=0)$ state, due to the location of the Ar along the NH_3 inversion coordinate. In any case, even if the NH_3 subunit is not freely inverting, an energy level could shift by no more than ~ 12 GHz (0.4 cm^{-1}) as a result of total quenching, and this small change would not significantly change the angular PES.

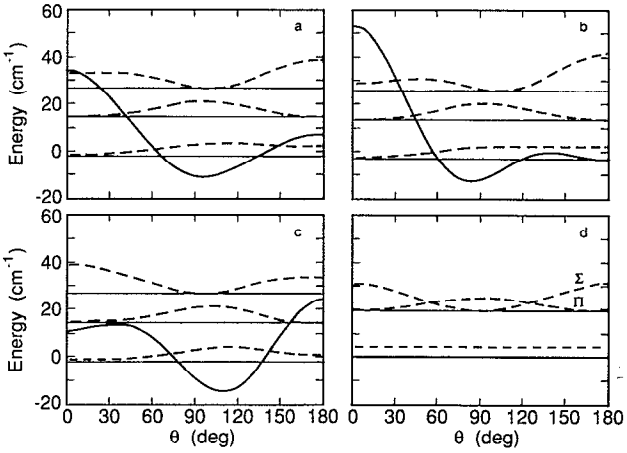

FIG. 7. Potential energy surfaces (heavy solid curves), vibrational energy levels (solid horizontal lines), and squared wave functions (dotted curves) for $0° \leqslant \theta \leqslant 180°$. The best fit ($V_{30}$ fixed at 3 cm^{-1}) is shown in (a), and the fits with $V_{30} = \pm 15$ are shown in (b) and (c), respectively. In (d) the results for an isotropic potential are shown for comparison.

Let us now consider the surfaces, wavefunctions, and energy levels plotted in Figs. 7(a), 7(b), and 7(c). We will discuss the expansion coefficients in terms of the constraints imposed by the measured surface, namely, that V_{30} is unknown and is allowed to vary considerably, that V_{10} is roughly half the size of V_{20}, and that V_{10} and V_{20} are well-determined for any given value of V_{30}. The fact that V_{20} is large relative to V_{10} and positive implies that there is a global minimum near $\theta = 90°$, which causes the $\Pi(1_0,n=0)$ state, localized in the region with θ near 90°, to be lower in energy than the $\Sigma(1_0,n=0)$ state, which itself is localized with θ near 0° and 180°.

The sign and magnitude of V_{30} relative to V_{10} are dominant effects in determining the shape of the angular potential surface. When both have the same sign, V_{30} reinforces V_{10} and eventually induces a large barrier at $\theta = 0°$ or 180° and a secondary minimum 180° from the barrier. Conversely, when they are of opposite sign, V_{30} tends to cancel V_{10}, leaving V_{20} to dominate the surface with a minimum near $\theta = 90°$.

The location of the global minimum in the surface, always localized near the T-shaped configuration ($\theta = 90°$), ranges from $\theta = 84°$ to 110° as V_{30} varies from 15 cm^{-1} to -15 cm^{-1} [Figs. 7(b) and 7(c)]. Over this range the RMSD is essentially constant (Fig. 6), and any set of V_{10}, V_{20}, and V_{30} that minimize the RMSD chosen in this range describes the surface equally well. Since V_{10} was arbitrarily constrained to be positive, we must also consider the corresponding range of supplementary angles ($\theta = 70°$ to 96°) wherein the minimum would be found if V_{10} were constrained to be negative. Averaged over the zero-point vibrations, the NH_3 monomer has 1.012 Å N–H bond lengths and 106.7° H–N–H bond angles;[28] the N–H bond thus makes a 67.9° angle with the NH_3 symmetry axis. We note that a positive V_{10} favors weak bonding in the region between the N–H bond and the lone pair on the nitrogen, while a negative V_{10} favors bonding in the region closer to the hydrogens. Without any information on V_{33}, it is not possible to characterize the anisotropy in the surface as a function of rotation of the NH_3 about its symmetry axis.

The experimental potential surface contains contributions from the effects of induction, dispersion, and repulsion. The most direct way to determine the contribution from these effects is to evaluate each of them in terms of the appropriate angular coordinates. The general form of the contribution from the induction or dispersion energy, through R^{-10}, is given by

$$V^{\text{ind/disp}}(R,\theta,\chi) = \sum_{0\leqslant\mu\leqslant\lambda}\left(-\sum_{n=6}^{10}\frac{C_n^{\lambda\mu}}{R^n}\right)[C_{\lambda\mu}(\theta,\chi) + (-1)^{\mu}C_{\lambda-\mu}(\theta,\chi)](1+\delta_{\mu 0})^{-1}. \tag{24}$$

TABLE IV. Analytic expressions for the induction coefficients of Ar–NH_3.

λ	μ	$C_6^{\lambda\mu}$	$C_7^{\lambda\mu}$	$C_8^{\lambda\mu}$	$C_9^{\lambda\mu}$	$C_{10}^{\lambda\mu}$
0	0	$\alpha\mu^2$		$(3/2)\alpha\Theta^2$		$2\alpha\Omega^2$
1	0		$(18/5)\alpha\mu\Theta$		$(36/7)\alpha\Theta\Omega_{30}$	
2	0	$\alpha\mu^2$		$(12/7)\alpha[\Theta^2+3\mu\Omega_{30}]$		$(25/21)\alpha[2\Omega_{30}^2-5\Omega_{33}^2]$
3	0		$(12/5)\alpha\mu\Theta$		$4\alpha\Theta\Omega_{30}$	
3	3				$5\alpha\Theta\Omega_{33}$	
4	0			$(1/7)\alpha[9\Theta^2+20\mu\Omega_{30}]$		$(162/77)\alpha[\Omega_{30}^2+\Omega_{33}^2]$
4	3			$-5(1/7)^{1/2}\alpha\mu\Omega_{33}$		$(162/11)(1/7)^{1/2}\alpha\Omega_{30}\Omega_{33}$
5	0				$(20/7)\alpha\Theta\Omega_{30}$	
5	3				$-4(1/7)^{1/2}\alpha\Theta\Omega_{33}$	
6	0					$(5/33)\alpha[10\Omega_{30}^2-\Omega_{33}^2]$
6	3					$-(10/11)(7/3)^{1/2}\alpha\Omega_{30}\Omega_{33}$
6	6					$5(7/33)^{1/2}\alpha\Omega_{33}^2$

The notation of Eq. (24) warrants some explanation: $C_n^{\lambda\mu}$ refers to an induction or dispersion coefficient, whereas $C_{\lambda\mu}(\theta,\chi)$ refers to the $\lambda\mu$th renormalized spherical harmonic. Analytic expressions for the induction coefficients including all terms up to octopole-induced dipole, are evaluated in the Appendix, and tabulated in Table IV. The values of the molecular constants used in Table IV are collected in Table V. The coefficients for the dispersion energy including terms up to R^{-10}, are obtained by scaling the dispersion coefficients calculated for He–NH_3 and Ne–NH_3,[20] according to the polarizability of the rare gas atom ($\alpha_{He}=1.390\,a_0^3$, $\alpha_{Ne}=2.672\,a_0^3$, and $\alpha_{Ar}=11.08\,a_0^3$) and taking their average. The results of scaling He–NH_3 vs Ne–NH_3 agree to at least 30% (typically better than 10%). We can estimate that the scaled coefficients are accurate to about 20% by comparing the scaled C_6^{00} coefficient ($92.7\,Ha_0^2$) to that obtained by combining the C_6^{00} coefficients of NH_3 and Ar[34] ($75.2\,Ha_0^2$). The scaled coefficients are then converted from the definition of dispersion energy used in Ref. 20 to the expansion shown in Eq. (24) with the relation

$$C_n^{LK}=(-1)^{L+K}(2L+1)^{-1/2}C_n^{LKOOL}. \tag{25}$$

The dispersion coefficients, in atomic units, are given in Tables VI.

The attractive contribution to the surface, denoted V^{attr}, is simply the sum of V^{ind} and V^{disp}. Table VII presents $V_{\lambda\mu}^{ind}$, $V_{\lambda\mu}^{disp}$, and $V_{\lambda\mu}^{attr}$ which are the renormalized spherical harmonic expansion coefficients obtained by evaluating

$$V_{\lambda\mu}^{ind/disp/attr}=\left(-\sum_{n=6}^{10}\frac{C_n^{\lambda\mu}}{R^n}\right) \tag{26}$$

TABLE V. Molecular constants used for induction coefficients.

Molecule	Constant	Value	Reference
Ar	α	$11.08\,a_0^3$	31
NH_3	μ	$0.57892\,ea_0$	28
	Θ	$-1.725\,ea_0^2$	31
	Ω_{30}	$-1.69\,ea_0^3$	31
	Ω_{33}	$-1.72\,ea_0^3$	31
	Ω^a	$2.96\,ea_0^3$	31

[a] $\Omega^2=\Omega_{30}^2+2\Omega_{33}^2$.

at $R=7.2359\,a_0$, and converted to cm^{-1}. It is seen that dispersion interactions dominate the attractive contribution to the surface, and that at the experimentally observed intermolecular separation the expansion in renormalized spherical harmonics is reasonably converged. Cursory inspection of Table VII reveals there are important attractive contributions to the surface through V_{43}^{attr}, with particularly large contributions from V_{33}^{attr} and V_{43}^{attr}. If the relative magnitudes of the $V_{\lambda\mu}^{attr}$ are indicative of the importance of the experimentally determined coefficients ($V_{\lambda\mu}^{expt}$), then experimentally determined coefficients must be obtained through V_{43}^{expt} before a term by term comparison can be made between V^{expt} and V^{attr} in order to extract the repulsive contribution to the surface (V^{rep}). Without data that are explicitly dependent on the higher order terms, we can only determine *effective* $V_{\lambda\mu}^{expt}$ coefficients that depend on the values at which the higher order coefficients have been fixed, as already discussed in Sec. IV. Future work will therefore include determination of the V_{30}^{expt}, V_{33}^{expt}, V_{40}^{expt}, and V_{43}^{expt} coefficients through measurement of E state transitions between 35 cm^{-1} and 50 cm^{-1} that correlate with $j_k=2_1\leftarrow1_1$ and $2_2\leftarrow1_1$ of the monomer.

It is interesting to compare our results with the *ab initio* surface calculated by Chałasiński *et al.*[18] and the properties of the surface calculated by van Bladel *et al.*[19] In order to use

TABLE VI. Dispersion coefficients of Ar–NH_3 expressed in atomic units.[a]

λ	μ	$C_6^{\lambda\mu}$	$C_7^{\lambda\mu}$	$C_8^{\lambda\mu}$	$C_9^{\lambda\mu}$	$C_{10}^{\lambda\mu}$
0	0	92.7		1987		47090
1	0		−220		−5472	
2	0	−1.8		875		46720
3	0		175		19170	
3	3		241		23720	
4	0			−245		−23670
4	3			−1005		−83030
5	0				−2510	
5	3				−362	
6	0					264
6	3					6378
6	6					5480

[a] Obtained by scaling the coefficients given for He–NH_3 and Ne–NH_3 in Ref. 20.

TABLE VII. Induction and dispersion contributions to the potential energy of Ar–NH_3 expressed as coefficients of an expansion in renormalized spherical harmonics and evaluated at $R = 7.2359\,a_0$ and converted to cm^{-1} [see Eqs. (24) and (26)].

$\lambda\mu$	$V_{\lambda\mu}^{ind}$	$V_{\lambda\mu}^{disp}$	$V_{\lambda\mu}^{attr}$
00	−7.2	−225.5	−232.7
10	7.8	68.3	76.1
20	−5.6	−48.8	−54.4
30	5.1	−114.2	−109.1
33	−0.7	−146.4	−147.1
40	−0.4	20.3	19.9
43	−0.7	75.5	74.8
50	−0.4	10.1	9.7
53	0.2	1.5	1.7
60	0.0	−0.2	−0.2
63	0.0	−3.5	−3.5
66	−0.1	−3.0	−3.1

the results of Chałasiński *et al.*[18] we parameterized their "best" [the $\Delta E(2)$] and their "second best" (SCF + D) surfaces as expansions in $C_{\lambda\mu}(\theta,\chi)$, and predicted energy levels and other properties of the complex. Van Bladel *et al.*[19] did not actually describe their surface, but the calculated energy levels and other properties of the complex were given. We compare the results of these two calculations with our experimental results in Table VIII. Chałasiński *et al.*[18] state that their SCF + D surface is too flat (i.e., not anisotropic enough), but it actually fits the data as well as $\Delta E(2)$. The primary reason for this is that the $\Delta E(2)$ surface is too anisotropic; over the range of θ and χ, it varies by about 105 cm^{-1}, whereas the SCF + D surface varies by about 63 cm^{-1}, while the experimentally determined surface varies by 40 cm^{-1} to 66 cm^{-1} (depending on the value of V_{30}).

Clearly, neither of the *ab initio* surfaces can adequately represent all of the measured properties of the Ar–NH_3 complex. The present work, and the efforts currently in progress to measure and assign the VRT spectra of the E states of this complex, should be of significant value for future efforts to improve the agreement between theory and experiment.

TABLE VIII. Comparison of experimental results with *ab initio* calculations.

Quantity	Experiment[a]	Ref. 18 SCF + D	Ref. 18 $\Delta E(2)$	Ref. 19
Σ bend (cm^{-1})	26.47	32.1	43.6	24.1
Π bend (cm^{-1})	16.59	18.0	16.7	21.2
$\Sigma(0_0, n=0)$ dipole (D)	0.261[b]	0.501	0.521	0.577
$\Sigma(0_0, n=0)$ eqQ_{aa} (MHz)	0.350[b]	0.11	0.33	−0.22
$\Sigma(1_0, n=0)$ eqQ_{aa} (MHz)	−0.84	−1.09	−0.73	−0.82
$\Pi(1_0, n=0)$ eqQ_{aa} (MHz)	0.92	0.88	0.94	0.76

[a] This work.
[b] Reference 15.

ACKNOWLEDGMENTS

This work was supported by NSF Grant No. CHE86-12296. R.C.C. is supported by the U.S. Department of Energy. The authors wish to thank A. van der Avoird for making the results of his calculations available to us prior to publication and for interesting discussions.

APPENDIX

The expression for the spherical harmonic expansion coefficients for the induction energy of a nonlinear molecule–spherical molecule system is given in Eq. (2.203) of Ref. 31. It is

$$u_{l_1'\alpha l_1''}(l_1 0 l_1; n_1 0; r) = \tfrac{1}{2}(4\pi)^{3/2}\left[\frac{(l_1'+1)(l_1''+1)(2l_1'+3)(2l_1''+3)}{(2l_1+1)}\right]^{1/2} \times C(l_1'+1\,l_1''+1\,l_1;000)\begin{Bmatrix} l_1' & l_1'+1 & 1 \\ l_1''+1 & l_1'' & l_1 \end{Bmatrix} \times r^{-(l_1'+l_1''+4)}\alpha_2 \sum_{n_1'n_1''} C(l_1'l_1''l_1;n_1'n_1''n_1)\mathcal{Q}_{l_1'n_1'}\mathcal{Q}_{l_1''n_1''} \tag{A1}$$

where $\{:::\}$ is a 6-j symbol, $C(...;...)$ is a Clebsch–Gordon coefficient, $\mathcal{Q}_{l_1 n_1}$ is the body-fixed spherical multipole moment of the nonlinear molecule, and α_2 is the body-fixed irreducible polarizability of the spherical molecule. The Clebsch–Gordon coefficients place some restrictions on which terms are allowed to be nonzero. Notably, $C(l_1'+1\,l_1''+1\,l_1;0\,0\,0)$ will be zero if $(l_1'+l_1''+l_1)$ is odd, $C(l_1'l_1''l_1;n_1'n_1''n_1)$ will be zero if l_1', l_1'', and l_1 do not satisfy the triangle relation or if $n_1'+n_1''\neq n_1$. Furthermore, it is seen that the r^{-n} dependence will have n even when l_1 is even, and n odd when l_1 is odd.

The renormalized spherical harmonic expansion coefficients (Table IV) are then

$$C_n^{lm} = (-1)^m r^n \sqrt{\frac{2l+1}{4\pi}} \sum_{l_1'l_1''} - u_{l_1'\alpha l_1''}(l0l;m0;r), \tag{A2}$$

where l_1', l_1'', and l satisfy the triangle relation and $l_1'+l_1''+4=n$. For Ar–NH_3 all allowed combinations of $\mathcal{Q}_{10}$, $\mathcal{Q}_{20}$, $\mathcal{Q}_{30}$, and $\mathcal{Q}_{3\pm3}$ (dipole, quadrupole, and octopole) were included.

[1] J. M. Hutson, J. Chem. Phys. **89**, 4550 (1988).
[2] R. C. Cohen and R. J. Saykally, J. Phys. Chem. **94**, 7991 (1990).
[3] J. M. Hutson, J. Chem. Phys. **92**, 157 (1990).
[4] G. T. Fraser, F. J. Lovas, R. D. Suenram, D. D. Nelson, Jr., and W. Klemperer, J. Chem. Phys. **84**, 5983 (1986).
[5] G. T. Fraser, D. D. Nelson, Jr., K. I. Perterson, and W. Klemperer, J. Chem. Phys. **84**, 2472 (1986).
[6] G. T. Fraser, K. R. Leopold, and W. Klemperer, J. Chem. Phys. **81**, 2577 (1984).
[7] G. T. Fraser, K. R. Leopold, and W. Klemperer, J. Chem. Phys. **80**, 1423 (1984).
[8] G. T. Fraser, K. R. Leopold, D. D. Nelson, Jr., A. Tung, and W. Klemperer, J. Chem. Phys. **80**, 3073 (1984).
[9] B. J. Howard (unpublished).
[10] P. Herbine and T. R. Dyke, J. Chem. Phys. **83**, 3768 (1985).
[11] G. T. Fraser, D. D. Nelson, Jr., G. J. Gerfen, and W. Klemperer, J. Chem. Phys. **83**, 5442 (1985).

[12]D. D. Nelson, Jr., G. T. Fraser, and W. Klemperer, J. Chem. Phys. **83**, 6201 (1985).
[13]M. Havenith, R. C. Cohen, K. L. Busarow, D. H. Gwo, Y. T. Lee, and R. J. Saykally, J. Chem. Phys. (submitted).
[14]G. T. Fraser, D. D. Nelson, Jr., A. C. Charo, and W. Klemperer, J. Chem. Phys. **82**, 2535 (1985).
[15]D. D. Nelson, Jr., G. T. Fraser, K. I. Peterson, K. Zhao, W. Klemperer, F. J. Lovas, and R. D. Suernam, J. Chem. Phys. **85**, 5512 (1986).
[16]D. H. Gwo, M. Havenith, K. L. Busarow, R. C. Cohen, C. A. Schmuttenmaer, and R. J. Saykally, Mol. Phys. **71**, 453 (1990).
[17]H. Meyer, U. Buck, and R. Schinke, J. Chem. Phys. **84**, 4976 (1986).
[18]G. Chałasiński, S. M. Cybulski, M. M. Szczęśniak, and S. Scheiner, J. Chem. Phys. **91**, 7809 (1989).
[19]J. W. I. van Bladel, A. van der Avoird, and P. E. S. Wormer, J. Chem. Phys. **94**, 501 (1991).
[20]W. Rijks and P. E. S. Wormer, J. Chem. Phys. **92**, 5754 (1990); *ibid.* **90**, 6507 (1989). The coefficients used in the present paper are those from the untruncated tables provided by the above authors as described in J. Chem. Phys. **92**, 5754 (1990).
[21]C. H. Townes and A. L. Schawlow, *Microwave Spectroscopy* (Dover, New York, 1975), Chap. 3; G. Herzberg, *Infrared and Raman Spectra of Polyatomic Molecules* (Van Nostrand Reinhold, New York, 1945), Chap. 4.
[22]P. R. Bunker, *Molecular Symmetry and Spectroscopy* (Academic, New York, 1979).
[23]B. J. Howard, Symposium on "Atomic and Molecular Clusters: Spectroscopy, Structure and Dynamics," at the ACS National Meeting, Miami, Florida, 1989.
[24]E. Zwart, H. Linnartz, W. Leo Meerts, G. T. Fraser, D. D. Nelson, Jr., and W. Klemperer, J. Chem. Phys. (to be published).
[25]G. A. Blake, K. B. Laughlin, R. C. Cohen, K. L. Busarow, D. H. Gwo, C. A. Schmuttenmaer, D. W. Steyert, and R. J. Saykally, Rev. Sci. Instrum. (in press).
[26]H. P. Benz, A. Bauder, and Hs. H. Günthard, J. Mol. Spectrosc. **21**, 156 (1966).
[27]R. L. Robinson, Ph. D. thesis, University of California, Berkeley, 1987.
[28]M. D. Marshall and J. S. Muenter, J. Mol. Spectrosc. **85**, 322 (1981).
[29]F. A. Baiocchi, T. A. Dixon, C. H. Joyner, and W. Klemperer, J. Chem. Phys. **75**, 2041 (1981).
[30]K. T. Tang, J. M. Norbeck, and P. R. Certain, J. Chem. Phys. **64**, 3063 (1976); E. A. Reinsch and W. Meyer, Phys. Rev. A **14**, 915 (1976).
[31]C. G. Gray and K. E. Gubbins, *Theory of Molecular Fluids* (Clarendon, Oxford, 1984), Vol. 1.
[32]R. L. Poyter, H. M. Pickett, and E. A. Cohen, *Submillimeter, Millimeter, and Microwave Spectral Line Catalog.*
[33]R. J. LeRoy and J. M. Hutson, J. Chem. Phys. **86**, 837 (1987).
[34]A. D. Buckingham, P. W. Fowler, J. M. Hutson, Chem. Rev. **88**, 963 (1988).